

Three-dimensional high-resolution imaging of cardiac proteins to construct models of intracellular Ca^{2+} signalling in rat ventricular myocytes

Christian Soeller¹, Isuru D. Jayasinghe¹, Pan Li², Arun V. Holden³ and Mark B. Cannell¹

¹Department of Physiology, School of Medical Sciences, University of Auckland, Private Bag 92019, Auckland, New Zealand

²Center for Biomedical Computing, Simula Research Laboratory, Martin Linges Vie 17, Fornebu, Norway

³Institute of Membrane and Systems Biology, Faculty of Biological Sciences, University of Leeds, Leeds LS2 9JT, UK

Quantitative understanding of the Ca^{2+} handling in cardiac ventricular myocytes requires accurate knowledge of cardiac ultrastructure and protein distribution. We have therefore developed high-resolution imaging and analysis approaches to measure the three-dimensional distribution of immunolabelled proteins with confocal microscopy. Labelling of single rat cardiac myocytes with an antibody to the Z-line marker α -actinin revealed a complex architecture of sarcomere misalignment across single cells. Double immunolabelling was used to relate the Z-line structure to the distribution of ryanodine receptors (RyRs, the intracellular Ca^{2+} release channels) and the transverse tubular system. Both RyR and transverse tubular system distributions exhibited frequent dislocations from the simple planar geometry generally assumed in existing mathematical models. To investigate potential effects of these irregularities on Ca^{2+} dynamics, we determined the three-dimensional distribution of RyR clusters within an extended section of a single rat ventricular myocyte to construct a model of stochastic Ca^{2+} dynamics with a measured Ca^{2+} release unit (CRU) distribution. Calculations with this model were compared with a second model in which all CRUs were placed on flat planes. The model with a realistic CRU distribution supported Ca^{2+} waves that spread axially along the cell at velocities of $\sim 50 \mu\text{m s}^{-1}$. By contrast, in the model with planar CRU distribution the axial wave spread was slowed roughly twofold and wave propagation often nearly faltered. These results demonstrate that spatial features of the CRU distribution on multiple length scales may significantly affect intracellular Ca^{2+} dynamics and must be captured in detailed mechanistic models to achieve quantitative as well as qualitative insight.

(Received 21 October 2008; accepted after revision 2 January 2009; first published online 12 January 2009)

Corresponding author C. Soeller: Department of Physiology, School of Medical Sciences, University of Auckland, Private Bag 92019, Auckland, New Zealand. Email: c.soeller@auckland.ac.nz

In cardiac ventricular myocytes, the increase in intracellular Ca^{2+} produced by membrane depolarization (during the cardiac action potential) is initiated by a small Ca^{2+} influx from voltage-sensitive Ca^{2+} channels in the surface membrane. This triggers a larger release of Ca^{2+} from the sarcoplasmic reticulum (SR) via Ca^{2+} -sensitive ryanodine receptors (RyRs; Franzini-Armstrong & Protasi, 1997) in a process known as Ca^{2+} -induced Ca^{2+} release (CICR; Fabiato, 1983, 1985), and the resulting increase in Ca^{2+} activates contraction. The RyRs are organized into clusters at junctions between the SR and the surface membrane to form functional signal transduction complexes. Stern and collaborators termed

these functional units in skeletal muscle ‘couplons’ (Stern *et al.* 1997), and this definition was later extended to cardiac muscle (Franzini-Armstrong *et al.* 1999). In ventricular muscle, the surface membrane invaginates the cell to carry excitation rapidly into the interior, and these invaginations are called the transverse tubular system (t-system; Forbes *et al.* 1984; Soeller & Cannell, 1999). Most couplons or ‘ Ca^{2+} release units’ (CRUs) are triggered (near synchronously) during the action potential, and spatiotemporal summation of thousands of microscopic release events, called Ca^{2+} sparks (Cheng *et al.* 1993), gives rise to the cell-wide Ca^{2+} transient. In some conditions (often related to an ‘overload’ of the SR with Ca^{2+}),

the release of Ca^{2+} can escape the tight control of membrane voltage and give rise to spontaneously triggered regenerative waves of Ca^{2+} that may underlie cardiac arrhythmias (Berlin *et al.* 1989; Lakatta & Guarnieri, 1993; Katta & Laurita, 2005; Venetucci *et al.* 2008).

Theoretical analysis shows that detailed knowledge of the three-dimensional (3-D) distribution of CRUs and related proteins is required to explain the regulation of SR release and the transition between tightly controlled and spontaneous regenerative behaviour (e.g. Izu *et al.* 2006). Quantitative methods to measure the distribution of RyRs and related proteins based on confocal microscopy have now been developed (e.g. Chen-Izu *et al.* 2006; Soeller *et al.* 2007), but previous models for cardiac excitation–contraction (EC) coupling have only used a simplified approximation to the real distribution of couplons.

Here we describe the three-dimensional organization of couplons and their relationship to the contractile machinery and transverse tubular system in rat cardiac myocytes. Using an extended three-dimensional data set that encompasses several sarcomeres, we illustrate that Z-disks are generally not flat but rather exhibit dislocations and that the couplon distribution and the t-system follow these dislocations. The measured distribution of CRUs in this data set was incorporated into a stochastic model of Ca^{2+} dynamics (Li *et al.* 2007) to study the propagation of Ca^{2+} waves with the measured couplon distribution.

Methods

Ethical information

Enzymatically isolated rat cardiac myocytes were prepared as described elsewhere (Evans & Cannell, 1997), using protocols approved by the University of Auckland Animal Ethics Committee. Briefly, Wistar rats weighing approximately 250 g were given a lethal injection of pentobarbitone (100 mg kg^{-1} , i.p.) and hearts quickly mounted on a Langendorff perfusion system. Five minutes of retrograde coronary perfusion with a nominally Ca^{2+} -free Tyrode solution (containing, mM: NaCl, 120; KCl, 5.4; Hepes, 10; pyruvate, 5; glucose, 20; and taurine, 20; pH adjusted to 7.4 with NaOH) at 37°C was followed by the addition of 4 U ml^{-1} protease (type I; Sigma, St Louis, MO, USA), 1 mg ml^{-1} collagenase (type II; Worthington, Lakewood, NJ, USA) and $100 \mu\text{M}$ CaCl_2 . After 10–12 min of enzyme treatment, the ventricles were cut free, chopped into small pieces and triturated. The resulting cell suspension was filtered and the Ca^{2+} concentration raised to 1 mM over a period of 5 min.

Preparation of fixed ventricular cells

Cells were fixed for 10 min at room temperature in phosphate-buffered saline (PBS) containing 2%

paraformaldehyde and washed for a further 10 min in fresh PBS. To image myocytes with high resolution in transverse optical sections, we employed a method developed by Chen-Izu *et al.* (2006). A suspension of fixed myocytes in PBS was mixed with a low-temperature-melting agarose ($<36^\circ\text{C}$) in PBS solution at 37°C to a final agar concentration of 3% and cooled to room temperature. Blocks ($2\text{--}3 \text{ mm}^3$) were cut and transferred to 36-well plates where immunolabelling was performed.

Indirect immunofluorescence labelling of isolated cells

Fixed cells were permeabilized using 0.1% Triton X-100 in PBS for 10 min and then blocked in a PBS solution containing 5% BSA, 2% NGS (Normal Goat Serum, catalogue no. 10000C, CALTAG, San Francisco, CA, USA) and 0.05% Triton X-100 for 1 h at room temperature. Cells were incubated with primary antibodies at 4°C overnight. The cells were washed three times in PBS for 2 h and then incubated with secondary antibodies overnight at 4°C . Unbound secondary antibodies were removed by three further 2 h washes at room temperature.

Antibodies and fluorescence labelling

A polyclonal rabbit antibody (AB2912-100; Abcam, Cambridge, UK) was used for labelling a sarcolemmal and t-tubular membrane protein, caveolin-3. Double-labelling control experiments with a mouse monoclonal antibody against caveolin-3 (SC-5310; Santa Cruz Biotechnology, Santa Cruz, CA, USA) showed near complete colocalization with the polyclonal antibody and also confirmed that the polyclonal antibody did not give rise to non-specific background labelling. Clusters of RyR2 were labelled using mouse monoclonal anti-RyR2 antibodies (clone C3-33) purchased from Affinity Bioreagents (Golden, CO, USA). To label Z-lines, a mouse monoclonal antibody (Sigma) against α -actinin was used (clone EA-53). The secondary antibodies were goat anti-rabbit Alexa 488-conjugated immunoglobulin G (IgG; Molecular Probes, Invitrogen, Penrose, Auckland, NZ), goat anti-mouse Alexa 488-conjugated IgG (Molecular Probes, Invitrogen) or goat anti-mouse Alexa 568 or Alexa 594-conjugated IgG (Molecular Probes, Invitrogen). As detailed elsewhere (Soeller *et al.* 2007), the primary α -actinin antibodies were labelled using a Zenon Alexa Fluor 488 goat anti-mouse IgG1 kit (Molecular Probes, Invitrogen) when used in conjunction with the mouse anti-RyR2 antibody. In order to label mitochondria, living cells were incubated for 30 min in Tyrode solution containing 1 mM Ca^{2+} and 50 nM Mitotracker Red CMX-Ros (Molecular Probes, Invitrogen) and washed once with fresh Tyrode solution prior to fixing with 4% paraformaldehyde and subsequent immunolabelling.

Agar blocks containing fluorescently labelled cells were further sliced into ~ 1 -mm-thick slices and placed into a chamber whose bottom was a number 1.5 glass coverslip. To improve optical resolution, the cut slices were embedded in a high-optical-density mounting medium consisting of a saturated sucrose solution (index of refraction ~ 1.49) to match the oil immersion objective used for imaging. The slices were placed in a chamber, whose bottom was a number 1.5 coverslip that was mounted on the translation stage of the confocal microscope.

Imaging

Fluorescence images were recorded with a Zeiss LSM410 laser scanning confocal microscope using a Zeiss $\times 63$ NA 1.25 oil-immersion objective. Alexa 488 and Alexa 568/594 fluorochromes were excited with an Ar⁺ 488 laser (Uniphase, San Jose, CA, USA) and a 543 nm He–Ne laser (Zeiss, Jena, Germany), respectively. Stacks of confocal sections (0.2 – 0.25 μm spacing between adjacent sections) were acquired for offline three-dimensional data processing. To enhance the data for further analysis, iterative constrained deconvolution was performed using a Richardson–Lucy algorithm as previously described (Soeller & Cannell, 1999). The point-spread function (PSF) of the microscope was determined by imaging 3-D stacks of 100 nm fluorescent latex beads (Molecular Probes, Invitrogen) in the medium used for mounting the cells.

Data analysis and visualization

Data analysis was performed with custom routines written in IDL (ITT, Boulder, CO, USA). The distribution of RyR clusters was determined using a cluster detection algorithm in which the location of punctate labelling was determined with an approach similar to that used to derive the location of Ca²⁺ sparks from line-scan images (Cannell *et al.* 1994; Kong *et al.* 2008) but modified for 3-D. One step of the iterative procedure consisted of cross-correlating the deconvolved data stack with the measured PSF and extracting the location and amplitude of the N largest local maxima in the correlation data (N was typically 5). The co-ordinates of the identified maxima were added to a co-ordinate list. To prevent the algorithm repeatedly identifying the same clusters, scaled copies of the PSF (based on the identified cluster signal) were subtracted from the data at each location, which effectively removed the signal associated with that cluster. The modified data set was then used as input for the next iteration.

The α -actinin labelling is present at the Z-line of myofibrils. In cells imaged along the long axis of the cell (optical axis of the microscope), resolution is relatively

poor and thus the labelling forms ~ 1 - μm -wide bands. To determine the longitudinal position of the myofibrillar Z-disks more accurately, we calculated the centroid positions of these bands by fitting Gaussian functions to the intensity profiles along the long axis of the cell. The labelled bands were replaced by one-pixel-wide centroids (pixel size of ~ 60 nm) along the axis of the cell. The resulting thin sheets of tightly localized α -actinin distribution were visualized in three-dimensions after moderate smoothing with a 80-nm-wide (full width at half maximum) smoothing kernel. Three-dimensional visualizations of the processed labelling data were generated by isosurface rendering using the freely available software package *opendx* (www.opendx.org).

Mathematical modelling

To simulate regenerative Ca²⁺ dynamics with a realistic model geometry, the experimentally determined spatial distribution of RyR clusters from an exemplar data set from a myocyte were incorporated into a three-dimensional model ventricular cell (Li *et al.* 2007). The simulated volume was $24 \mu\text{m} \times 24 \mu\text{m} \times 7.2 \mu\text{m}$, which was discretized into $120 \times 120 \times 36$ voxels for computation. Calcium release and regenerative propagation were modelled by spatially discrete CRUs, which were placed at the experimentally measured locations of RyR clusters. These CRUs stochastically released Ca²⁺ into the cytosolic volume with probabilities determined by the local $[\text{Ca}^{2+}]_i$. This simulated the saltatory activation of Ca²⁺ sparks, which have been proposed to underlie regenerative waves in overloaded myocytes (Cheng *et al.* 1996). Released Ca²⁺ was subject to cytosolic diffusion and re-uptake into the SR (see also Appendix: *model equations and parameters*). All simulations assumed reflective boundaries at the faces of the computational domain and across the sarcolemma.

We also constructed a second model in which all CRUs were placed on flat and non-branching Z-disks with the same lateral CRU distribution as given by our data. To closely mimic the general geometry of the experimental data set, the planes were put at an angle of 7.6 deg to the transverse axis of the computational domain. Previous studies have used Ca²⁺ diffusion coefficients between 100 (Langer & Peskoff, 1996) and 600 $\mu\text{m}^2 \text{s}^{-1}$ (Pratusevich & Balke, 1996). Here we used a diffusion coefficient, D_c , of 150 $\mu\text{m}^2 \text{s}^{-1}$ to model isotropic diffusion, which corresponds to the transverse mobility used by Izu *et al.* 2001. Calcium wave propagation was (robustly) initiated by setting $[\text{Ca}^{2+}]_i$ to 50 μM in a small region (compare also Fig. 5C and D) at the beginning of the simulation. The value of 50 μM was chosen because it reliably started waves; lower values led to many failures to initiate regenerative release, whereas higher values of the wave trigger gave essentially the same results (as expected for

a regenerative process). A numerical solver for the model equations was implemented in the programming language C, and the simulations were performed on a Lenovo T61P (Lenovo, Morrisville, NC, USA) with a 2.5 GHz Intel Core2 Duo central processing unit and 4 Gbytes memory. A computation run that simulates the evolution of $[Ca^{2+}]_i$ over 500 ms takes about 3 h on this computer. To visualize the time course and propagation of regenerative release, three-dimensional isosurfaces of $[Ca^{2+}]_i$ were superimposed on the distribution of CRUs to show

both the wavefronts and the interaction between CRUs. All simulations were repeated to verify that stochastic variations between runs were small.

Results

Distribution of couplons in rat cardiac myocytes

An example of RyR staining and related cellular structures in rat cardiac myocytes is shown in Fig. 1. In a longitudinal

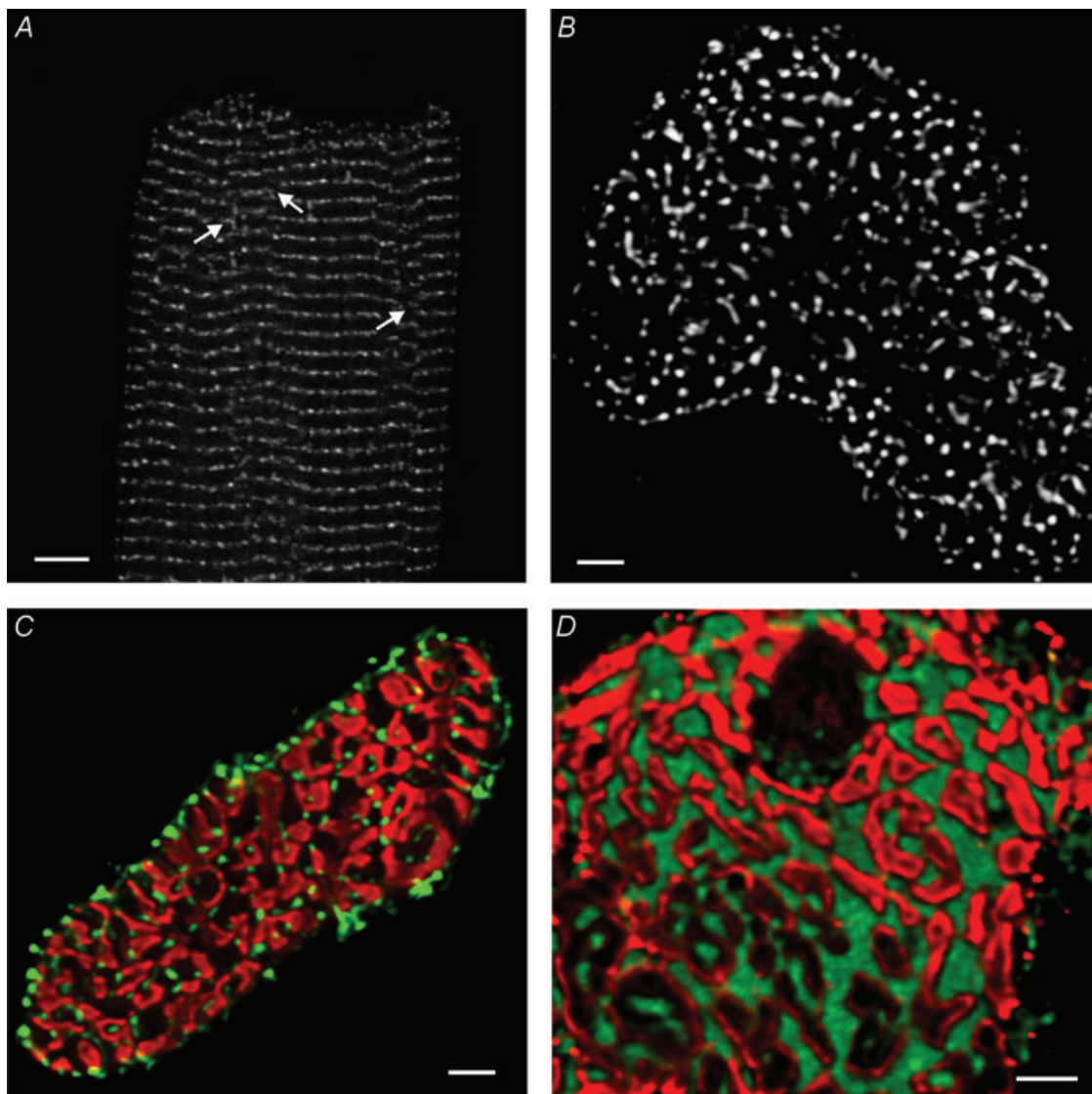


Figure 1. Immunofluorescence imaging of RyR clusters and Z-line architecture of myofibrils

A, in longitudinal confocal sections of myocytes, RyR labelling appeared as transverse arrays of densely spaced puncta. White arrows indicate regions where adjacent bands of RyR puncta appear to intersect. *B* shows a maximal intensity projection of the transverse RyR cluster distribution between two adjacent sarcomeres of a myocyte embedded in an agarose matrix. *C*, a similar projection of α -actinin labelling (red) outlines the shape of myofibrils in cross-section and the nature of the RyR cluster (green) arrangement around the contractile machinery. *D*, in cells labelled with a fixable mitochondrial marker, Mitotracker Red CMX-Ros (shown in green), strong labelling was observed in the intermyofibrillar regions that stained negative for α -actinin (red). Both α -actinin and Mitotracker labels were absent from the nuclear region (upper centre). Scale bars: *A*, 5 μ m; and *B–D*, 2 μ m.

confocal section through a cell (where the cell long axis is orthogonal to the microscope optical axis), the RyR labelling appears as bands of dense puncta (Fig. 1A). It is notable that in several regions of the image, bands appear to intersect so that the RyRs do not form a simple plane across the width of the cell. The detailed distribution of RyRs becomes much clearer in a cell imaged in transverse section (i.e. the cell is standing on-end and aligned with the axis of the microscope objective; Fig. 1B). In this transverse view, the RyR labelling generally appears as well-separated puncta distributed over the cross-section of the myocyte with an irregular distribution. Most puncta have a near diffraction-limited diameter of ~ 250 nm, although some larger structures are also present (Soeller *et al.* 2007). To clarify the relationship of RyR labelling to the contractile machinery, cells were simultaneously labelled for RyRs and the protein α -actinin, which anchors thin filaments at the Z-line. Figure 1C shows a transverse section centred on a Z-line, and it is apparent that the RyR puncta (green) are distributed around myofibrils revealed by the α -actinin labelling (red). This strongly suggests that the puncta of labelling correspond to RyR clusters or 'couplons', located at Z-lines. Myofibrils occupy less than 50% of the total cross-sectional area of the myocyte. Most of the remaining cross-sectional area was labelled positive with mitochondrial staining (green in Fig. 1D), consistent with the observation that the extramyofibrillar space is largely occupied by mitochondria (Page *et al.* 1971).

Z-Disk dislocations and transverse tubule system architecture

The dislocations in RyR labelling described above are also present in the architecture of Z-lines as visualized by α -actinin staining (Fig. 2). To clarify the relationship between t-system organization and Z-line dislocations, we double-labelled cells with a t-system marker using an antibody to the surface membrane protein caveolin-3, which is abundant in the t-system. Caveolin-3 labelling generally occurs in line with α -actinin staining, as might be expected from the known location of t-tubules at Z-lines in the heart (see Bers, 2001 for review). At Z-line dislocations, the t-system marker spans the dislocations so that the generally transverse orientation of tubules is changed to an axial orientation (Fig. 2A and B). Figure 2C illustrates another type of Z-line dislocation in a small section of a myocyte visualized by 3-D rendering. The Z-lines of myofibrils in this region branch and form a zig-zag band, effectively connecting adjacent sarcomeres along the length of the cell. An overlay of the Z-line label with the caveolin-3 label, shown in Fig. 2D, again demonstrates that the t-system closely follows the Z-line topology so that a complex three-dimensional pattern of interconnections in the axial direction is present.

Generation of an extended data set for mathematical modeling

Defining the three-dimensional architecture of Z-disks and RyR couplon distribution for input into a realistic mathematical model of Ca²⁺ handling requires accurate determination of the location of couplons and Z-lines. While imaging cells in the transverse direction provides high resolution within the plane of Z-disks (~ 250 nm) and provides accurate outlines of the contractile machinery, axial resolution is generally insufficient (~ 1 μ m). To overcome this limitation, we have used the idea that the centroid of an object can be determined with much better accuracy than the size of the object itself (provided the 'blurred' object is well separated from adjacent objects). Figure 3 shows the refinement of structure that can be achieved with this approach. The axial location of the local myofibrillar Z-lines was refined to within ~ 100 nm by calculating the centroid of α -actinin labelling (Fig. 3A). The improved precision of Z-line location data can be seen more clearly by comparing the 3-D organization of α -actinin labelling (red) with the refined data set (green; Fig. 3B). A similar approach was used to refine the location of couplons, and Fig. 3C shows an overlay of isosurface-rendered RyR data with detected couplon locations.

These localization techniques were used to analyse an extended 3-D data set of a cell double-labelled for α -actinin and RyRs. The data cover a volume of ~ 26 μ m \times 26 μ m \times 7.5 μ m from a region that was centred on a nucleus and spans more than three sarcomeres (Fig. 4A). The large hole in the Z-disk structure reflects the position of the nucleus, and dislocations in the Z-disk structure are illustrated in Fig. 4B and C. Figure 4B shows how couplons are arranged around the myofibril outline, while Fig. 4C shows the variability in axial position of the RyR clusters with respect to the Z-line and its dislocation. Figure 4D shows the distribution of RyR couplons within the volume. A histogram of nearest-neighbours distances between couplons (Fig. 4E) has a mean of 0.68 μ m, similar to that reported previously (Soeller *et al.* 2007). The variability in the axial RyR cluster positions and the frequent occurrence of dislocations in the Z-line pattern illustrated by this data set were seen in all cells inspected ($n > 20$). Regions containing dislocations extended typically over 10–20 sarcomeres, and several dislocated regions were seen in each myocyte (Soeller *et al.* 2007).

Stochastic modelling of Ca²⁺ handling

We used the centroids of the couplons in the volume (shown in Fig. 3) to provide co-ordinates for the location of CRUs in a spatially extended, stochastic model of intracellular Ca²⁺ handling (Li *et al.* 2007). Figure 5A

shows a perspective view, looking at the cell segment from the side, and the locations of Z-disks are apparent as bands of increased CRU density (white puncta). Most of the scattering in these bands arises from the variability in axial position of couplons as described in Fig. 4. This is made clearer by comparing Fig. 5A with Fig. 5B, in which the geometry was simplified to place couplons on flat planes which occupied the same general Z-line locations. Figure 5B also shows the extent to which couplon location is distorted by the perspective view, which is clearly minimal in the centre of the volume. By simulating a Ca^{2+} wave within the volumes shown in Fig. 5A and B we can examine the extent to which microscopic variations in couplon placement affect Ca^{2+} wave propagation.

Waves were initiated in these two models by starting the simulations with an elevated $[\text{Ca}^{2+}]_i$ of $50 \mu\text{M}$ in a small region, as shown by the isosurfaces at the top left of the volumes in Fig. 5C and D. The initiation and spread of this wave is shown by $[\text{Ca}^{2+}]_i$ isosurfaces shown in Fig. 5C–H. Comparison of the shape of these wave fronts shows that in flat Z-disks saltatory propagation occurs primarily along the Z-disk (Fig. 5D, F and H). However, the spread of the wave in the model with a measured CRU distribution (Fig. 5C, E and G) is more isotropic.

The spread of the Ca^{2+} wave along the axis of the cell is examined in more detail in Fig. 6. Figure 6A shows the distribution of $[\text{Ca}^{2+}]_i$ in space and the location of

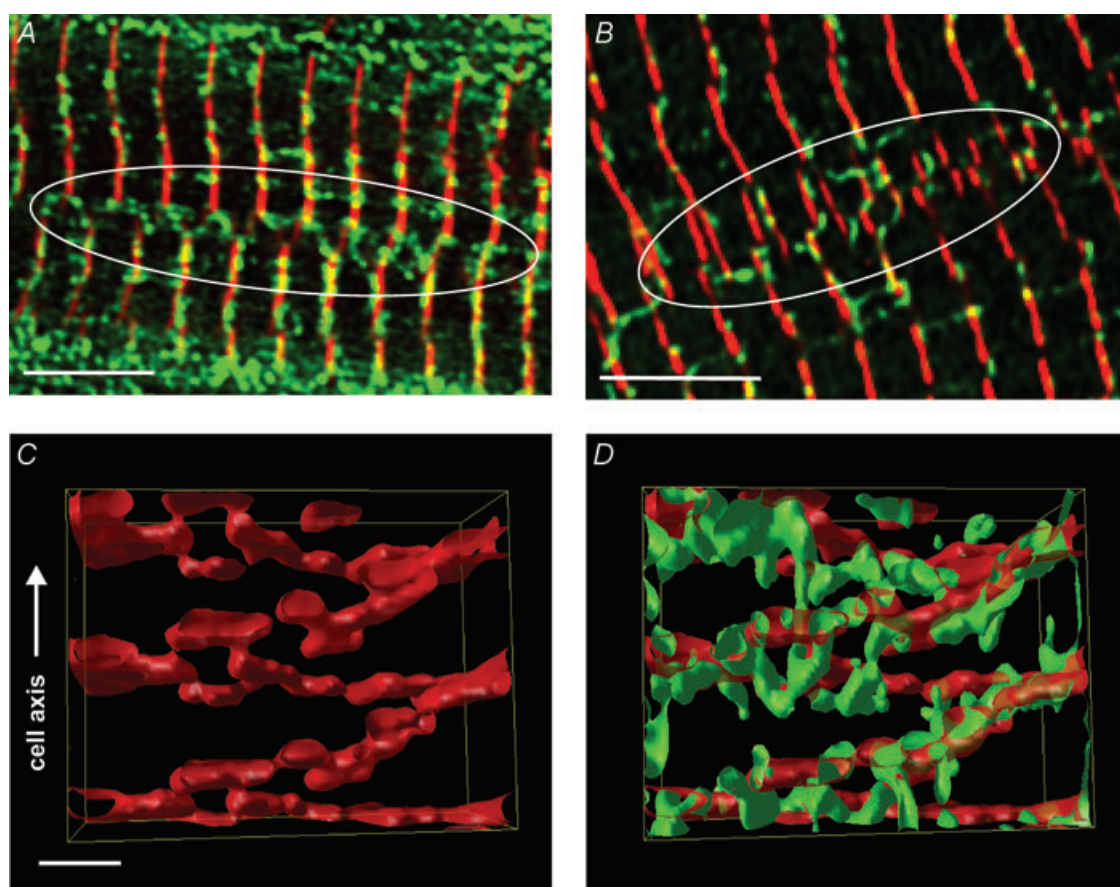


Figure 2. Longitudinal dislocations between Z-lines of neighbouring myofibrils and branching of the transverse tubular network

A and B, maximal intensity projections calculated from a shallow volume ($\sim 0.6 \mu\text{m}$ thick) of longitudinal confocal Z-stacks of cells labelled for α -actinin (red) and caveolin-3 (green). These illustrate examples of the misregistration of Z-lines between adjacent myofibrils that commonly span several sarcomeres (regions indicated by ovals) before returning into alignment. In this view, the t-tubule marker caveolin-3 (green) generally followed the planes of α -actinin staining but changed direction from transverse to axial or bifurcated in order to bridge misaligned Z-disks. Note that the punctate appearance of the caveolin stain at the cell periphery (A) reflects the non-uniform distribution of caveolin-3 on a projected part of the sarcolemma. C, a surface-rendered 3-D model of α -actinin labelling (red surface) illustrates a subcellular region with oblique arrangement of Z-lines (in relation to the longitudinal axis of the cell) that form a zig-zag-like pattern. D, an overlay of this 3-D image with caveolin-3 labelling (green surface) demonstrates that the network of transverse and axial tubules follows this zig-zag pattern. Scale bars: A and B, $5 \mu\text{m}$; and C, $1 \mu\text{m}$.

a line used to analyse CRU activation timing. Figure 6B shows simulated line-scan images of the rise in Ca²⁺ at various points along the line and mimic confocal line-scan images of Ca²⁺ waves (Cheng *et al.* 1996), albeit at a much higher spatial resolution since no blurring is present. The propagation of the wave fronts can be seen as a line connecting regions of similarly elevated Ca²⁺. In the model using the measured distribution of CRUs (Fig. 6B, left panel), Ca²⁺ release quickly spreads axially at a velocity of $\sim 50 \mu\text{m s}^{-1}$. However, when the distributions of CRUs within the Z-disk was assumed to be flat (Fig. 6B, right panel), propagation was much slower ($\sim 26 \mu\text{m s}^{-1}$) and appeared to falter as it moved between Z-disks (as seen by a gap in the wavefront). It is therefore clear that microscopic CRU location can have profound effects on the ability of Ca²⁺ waves to propagate within the cell.

Discussion

Distribution of couplons and related Z-line structures

The data presented here illustrate the complex Z-disk structure of isolated ventricular myocytes. As noted previously (Soeller *et al.* 2007), myofibrils stay in longitudinal register over limited distances and can develop dislocations. Three-dimensional visualization reveals that Z-disks exhibit prominent branches in some regions that effectively connect adjacent Z-disks. The RyR couplon distribution closely follows the Z-disk structure and therefore also exhibits dislocations, but there is additional variability in longitudinal location around the Z-disk. This microarchitecture reduces the effective axial distance between couplons and is an important factor in

the spread of regenerative Ca²⁺ release along the cell. In addition, the measured intercoulon distances are relatively small ($\sim 0.68 \mu\text{m}$), which promotes CRU firing by propagating CICR. Our measured spacing is smaller than was found in several previous studies (Cleemann *et al.* 1998; Kockskamper *et al.* 2001), a difference that may be ascribed to the increased resolution associated with the axial imaging we used. In connection with this point, we note that our measurements agree with those made with electron microscopy (Franzini-Armstrong *et al.* 1999).

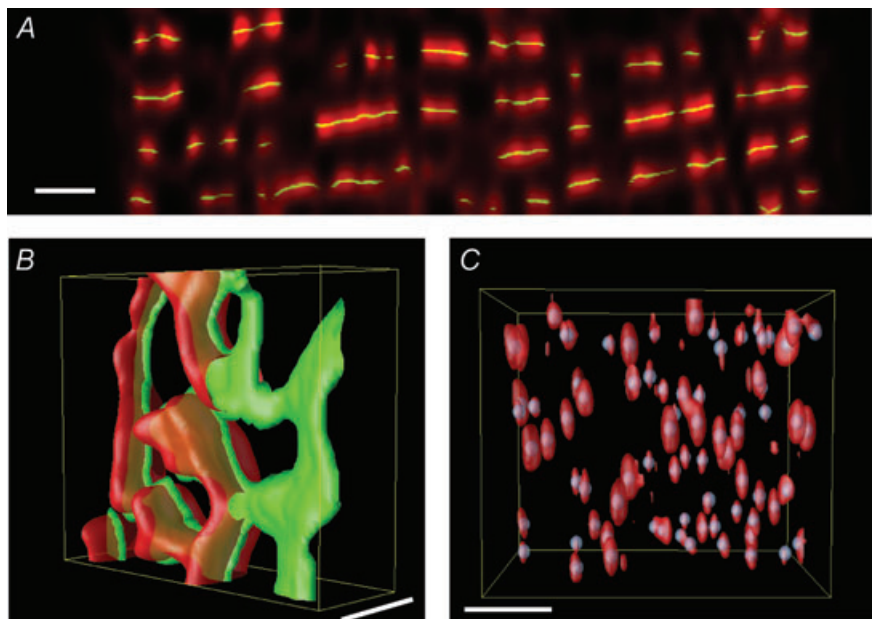
The t-system also exhibited dislocations in register with Z-disk dislocations. It is known that the t-system has axial components, the 'longitudinal' or 'axial' tubules, and is sometimes referred to as the 'transverse-axial tubular system' (TATS; see Sperelakis & Rubio, 1971; Soeller & Cannell, 1999). Our correlation of regions of abundant axial tubules to areas of Z-line dislocation is novel and provides insight into how the dislocated couplons are normally activated. Without axial tubules in this location, the dislocated CRUs would only be activated by propagating CICR, whereas with the t-system present, normal EC coupling can take place. The observation of branches in the t-system via obliquely running tubules may provide an additional pathway for axial solute movement and may be important in the case of putative accumulation/depletion of ions (Pásek *et al.* 2008) in the t-system.

Generation of models with realistic micro-architecture

A key point in mathematical modelling is the extent to which structure can be collapsed to simplify the complexity of the problem. In the case of Ca²⁺ signalling,

Figure 3. Determination of the location of RyR clusters and Z-lines at high resolution in 3-D

A, the pronounced axial blurring causes α -actinin to appear as thick transverse bands (red) in a single XZ plane. The axial centroids of these bands define the location of Z-lines with $\sim 100 \text{ nm}$ precision as shown in overlay (green). B, a surface-rendered 3-D image of the α -actinin (red surface) overlaid with the reconstructed Z-disk location (green) illustrates the resolution improvement in 3-D. C, a similar overlay between a 3-D image of RyR labelling (red) and the computed centroids (light blue) of detected RyR clusters. Scale bars: A, $2 \mu\text{m}$; B, $1.8 \mu\text{m}$; and C, $2 \mu\text{m}$.



at the level of a couplon, Ca^{2+} gradients on the scale of nanometres become important (Soeller & Cannell, 1997), while intercouplon signalling occurs on the scale of Ca^{2+} sparks, i.e. $\sim 1 \mu\text{m}$. However, our data show that the location of CRUs at the scale of $0.1 \mu\text{m}$ can affect Ca^{2+} wave propagation so that a detailed CRU location map can give quite different results from a simplified planar Z-line structure. It follows that a hierarchy of models is required to capture Ca^{2+} signalling in cells. At the next level of scale ($\sim 1 \mu\text{m}$), the dislocations of Z-lines become important, and intersarcomere wave propagation is also promoted by

these structures. We assume that models with measured micro-architecture provide realistic descriptions of signal gradients, and with non-linear signal transduction the magnitude and extent of such gradients become critical. Models of the type described here can be extended to examine other signal transduction processes, such as Ca^{2+} –calmodulin signalling (Mori *et al.* 2004), L-type Ca^{2+} channel Ca^{2+} -dependent inactivation (Peterson *et al.* 1999) and Na^{+} – Ca^{2+} exchanger (NCX) regulation (Bers & Ginsburg, 2007), and may therefore give new insight into cell function. However, without such modelling, we

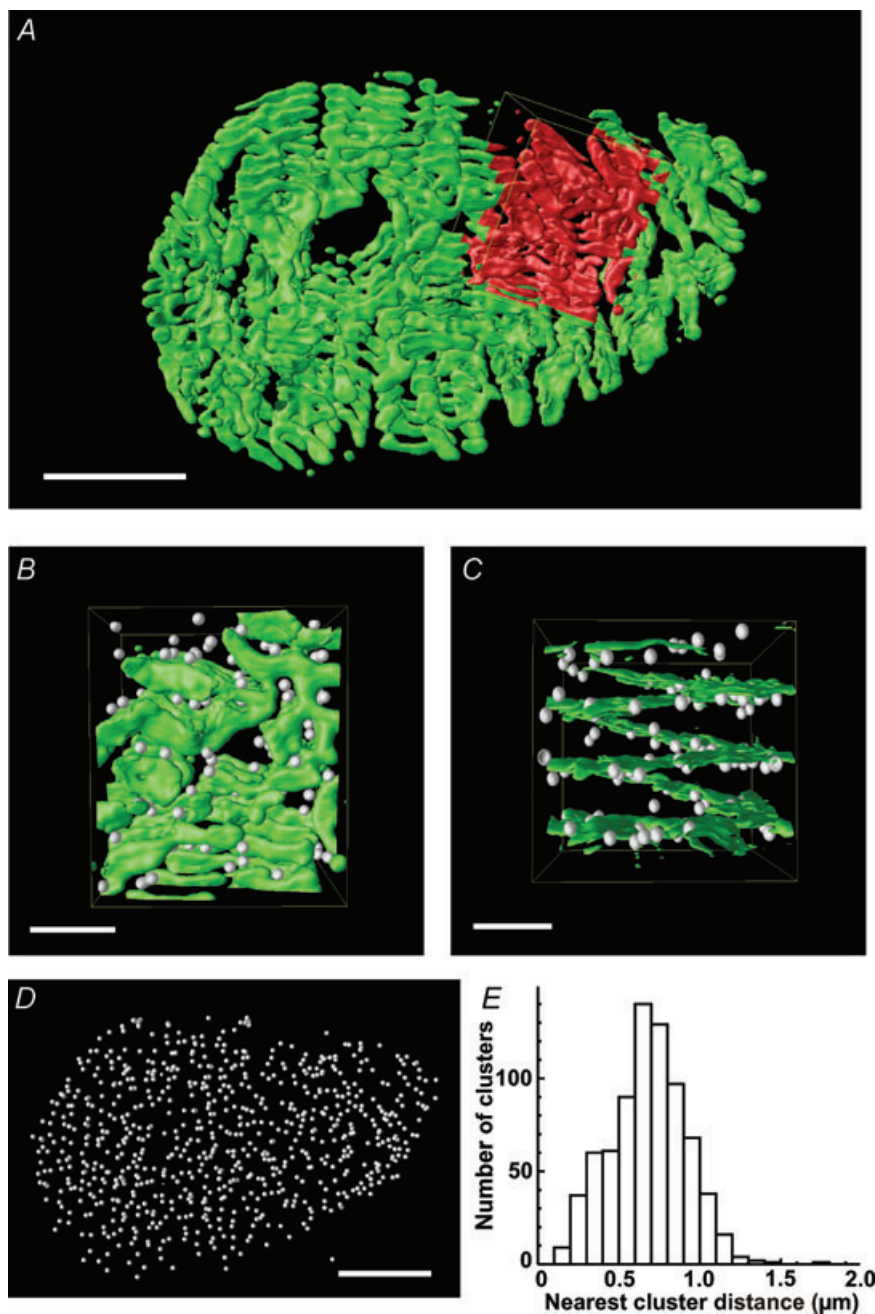


Figure 4. Three-dimensional reconstruction of Z-disks and location of RyR clusters in an extended volume through a ventricular myocyte

A shows a surface-rendered 3-D reconstruction of the Z-disks in a $\sim 26 \mu\text{m} \times 26 \mu\text{m} \times 7.5 \mu\text{m}$ volume encompassing ~ 4 sarcomeres of a myocyte labelled for α -actinin. The large circular gap marks the nuclear or perinuclear space, which is devoid of contractile machinery. The region indicated in red in A is shown in a transverse view of the cell in B, overlaid with detected RyR cluster centroids. A lateral longitudinal view (C) illustrates the close arrangement of couplons around the myofibrils near 3 consecutive Z-lines in an area of a prominent dislocation. D, a 3-D view of the RyR cluster centroids detected within the image volume. E, histogram of the three-dimensional distance to the nearest-neighbouring RyR cluster has a mean of $0.68 \mu\text{m}$. Scale bars: A, $5 \mu\text{m}$; B and C, $2 \mu\text{m}$; and D, $5 \mu\text{m}$.

cannot know what structural features can be collapsed or simplified without quantitatively or even qualitatively altering behaviour.

Wave propagation in rat ventricular myocytes

The presence of discrete CRUs as sources of local Ca²⁺ release gave rise to spatial non-uniformities in Ca²⁺

which were broadly compatible with experimentally observed non-uniformities in fluo-3- or fluo-4-loaded cells (Cannell *et al.* 1994). Variations in local CRU distribution and Z-disk structures across ventricular myocytes could provide a structural basis for points of failure of wave propagation (in regions lacking high CRU densities) as well as preferred locations of wave initiation (Berlin *et al.* 1989; Lipp & Niggli, 1993) in regions that

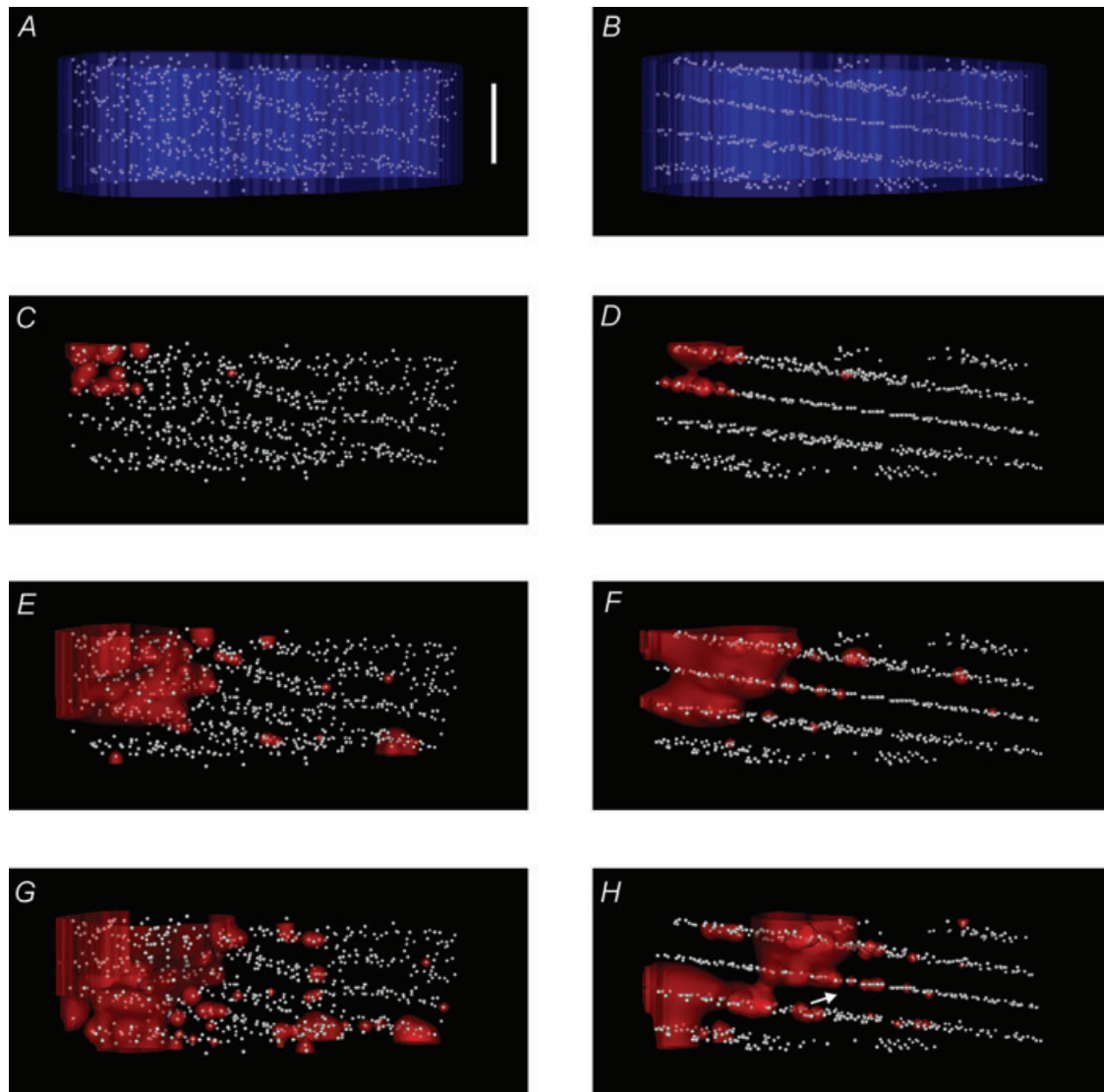


Figure 5. Integration of the CRU localization into a stochastic model of [Ca²⁺]_i dynamics

A, in a lateral longitudinal 3-D view of the cell, the model CRU distribution is shown and appears in this view organized into thick bands that reflect the local dislocations of adjacent Z-disks. B shows a similar view of a second model in which all CRUs were placed onto flat planes. A Ca²⁺ wave was initiated in the top left corner of both models by assigning a high local [Ca²⁺]_i (50 μM), as shown in C and D. The spread of the wavefront at the start of simulation and later times is illustrated by red 5-μM-[Ca²⁺]_i isosurfaces. The wave spread in the model with measured CRU distribution is shown in C, E and G, while D, F and H show wavefronts in the simplified model with planar CRU distribution. A largely isotropic spread of the wavefront was observed with the measured CRU distribution, in contrast to the spread mainly along Z-disks in the model with planar CRU distribution. Scale bar (applies to all panels), 5 μm. Simulation times: C and D, 1 ms; E and F, 85 ms; and G and H, 135 ms.

exhibit higher than average axial (and transverse) CRU densities. In any case, it is notable that the (more irregular) measured CRU distribution gave rise to more isotropic wave propagation compared with a model with idealized planar CRU distribution. In connection with this point, we note that the irregularity and dislocations that were present in the model with realistic CRU distribution were seen in all rat ventricular myocytes that we inspected (>20). Our model with a measured CRU distribution produced Ca^{2+} waves with realistic axial propagation velocities ($\sim 50 \mu\text{m s}^{-1}$), which are within the range recorded in experimental confocal line-scan images (e.g. $50\text{--}90 \mu\text{m s}^{-1}$; see Cheng *et al.* 1996). Velocities at the lower end of the experimental range are generally observed early in the genesis of waves, which was studied here, while velocities increase as the wave fully develops (Wussling & Salz, 1996). Previous models generally assumed faster diffusion in the axial direction (e.g. Izu *et al.* 2006) to produce realistic propagation behaviour in models with CRUs arranged in flat Z-disks. The recent high-resolution data provided by Bányász *et al.* 2007, shows that Ca^{2+} sparks are isotropic. We therefore used a more realistic model with isotropic Ca^{2+} diffusion, which is to our knowledge the first detailed model that incorporates this observation while producing waves that propagate reliably in the axial direction. While potential obstacles (such as mitochondria) could hinder diffusion in the transverse direction, detailed analysis of obstructed diffusion suggests that the degree of obstruction has to be quite severe to impede diffusion seriously. For example, a barrier that excludes 77% of the available space reduced the effective diffusion coefficient by only $\sim 11\%$ in detailed Monte-Carlo simulations of solute transport (Olviczky & Verkman, 1998). In any case, these considerations illustrate that further insight into the diffusion properties

of Ca^{2+} in intact myocytes is still required. Such information could be obtained, for example, by using optical 3-D-resolved photorelease from appropriate precursors in selected subcellular regions (Soeller *et al.* 2003).

By comparison, wave propagation in our second model, with planar CRU distribution, was much slower, and axial propagation often appeared to falter when assuming isotropic Ca^{2+} diffusion. Consistent with previous studies, we were able to improve longitudinal wave propagation in the model with flat Z-disks by doubling the axial Ca^{2+} diffusion coefficient (data not shown). The different behaviour between the planar model and the model with measured geometry is likely to be due to the effectively closer longitudinal spacing of CRUs in the measured geometry. While in both models Z-disks are $\sim 2 \mu\text{m}$ apart, the next-neighbour distance between CRUs within a 40° cone in the direction of longitudinal propagation is $\sim 10\%$ smaller in the measured geometry. This could explain the faster longitudinal wave velocity, v , in the measured geometry, because $v \approx D/d$, where d is the effective longitudinal CRU spacing and D the effective Ca^{2+} diffusion coefficient (Keizer *et al.* 1998). In the planar case, d may be close to the critical distance (Keizer *et al.* 1998) beyond which wave propagation is not supported, which is consistent with the faltering propagation that we observed. Given sufficient computing resources, it would be interesting to compare measured and planar geometries in a full-cell-sized model to study which of these models supports fully developed waves with spherical wavefronts as is generally experimentally observed (Wussling & Salz, 1996). Our results suggest that the planar model is unlikely to support the required isotropic wave spread, since propagation is much slower in the longitudinal direction than in the transverse direction along Z-disks.

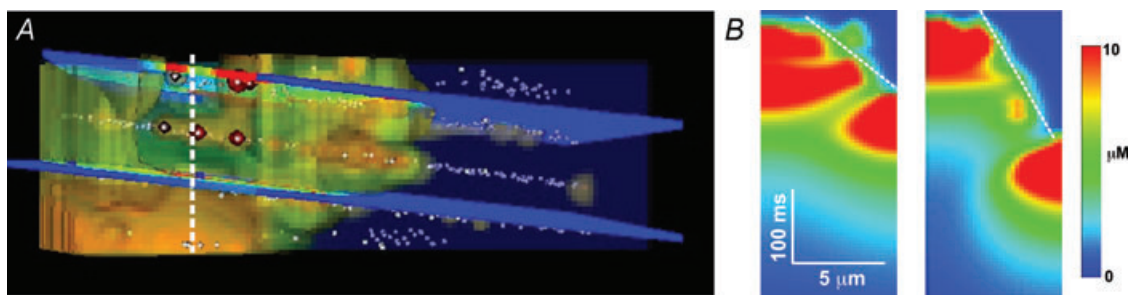


Figure 6. Effect of CRU arrangement on the propagation of Ca^{2+} waves

A, a 3-D view of the model shows the spread of a Ca^{2+} wave, which in the absence of the blurring introduced by a microscope, appears as a cloud with high-resolution detail. The white dots represent the CRUs. The thick dashed line marks the location of a line along the longitudinal axis of the cell from which a simulated line-scan image was generated. B, simulated line-scan images of the time course of $[\text{Ca}^{2+}]_i$ along the axis of the cell. The slope of the thin dashed lines joining two regions on consecutive Z-lines with $[\text{Ca}^{2+}]_i$ of $\sim 5 \mu\text{M}$ reflects the difference in the speed of axial propagation (~ 50 versus $\sim 26 \mu\text{m s}^{-1}$) in the measurement-based model (left) compared with the simplified model (right).

Table 1. Simulation parameters for stochastic simulations

Parameter	Standard value	Definition
D_c	150 $\mu\text{m}^2 \text{s}^{-1}$ (isotropic)	Cytosolic Ca ²⁺ diffusion coefficient
τ_R	10 ms	Open time of CRU
i_{Ca}	2 pA	Amplitude of CRU elemental Ca ²⁺ release
F	96 500 C mol ⁻¹	Farady's constant
v_{pump}	200 $\mu\text{M s}^{-1}$	Maximal SR pump rate
K_{pump}	0.184 μM	SR pump constant
m	4.0	SR pump Hill coefficient
n	1.6	Hill coefficient for CRU firing probability
C_0	0.10 μM	Background Ca ²⁺ concentration

Table 2. Ca²⁺ buffers in the model

	k_n^+ ($\mu\text{M}^{-1} \text{s}^{-1}$)	k_n^- (s^{-1})	$[B_n]_T$ (μM)	K_n (μM)
Calmodulin	100	38	24	0.38
Troponin C	39	20	70	0.51

Abbreviations: k_n^+ , on-rate; k_n^- , off-rate; $[B_n]_T$, total buffer concentration; K_n , Ca²⁺ binding constant.

Limitations of the mathematical model

Although the extended data set used in these simulations covered approximately four sarcomeres this is still only ~10% of the entire cell length. As a result, we only studied the initial phase of wave development. Effects seen in more fully developed waves (such as wave front curvature-dependent propagating velocities) were not investigated because of the reflection of Ca²⁺ at the axial boundaries of the simulation space. This limitation could be overcome in the future by employing objectives combining long working distance with high numerical apertures to record more axially extended data sets. Alternatively, axially extended data sets may be constructed by combining or repeating smaller, measured data sets. In combining these data sets it is crucial to avoid artefacts at axial interfaces between data sets. This requires a more complete characterization of the range of topological features in CRU distribution and Z-line architecture at the multiple scales important for Ca²⁺ signalling.

For simplicity our model did not consider CRUs as anything other than point sources. It is likely that if extended CRUs were included, waveform non-uniformity might be reduced. Additional factors that could affect wave propagation are variations in CRU excitability and CRU release flux between sites, which depends on local SR structure and the number of RyRs in a CRU. Some of these structural variables may now be measured using quantitative confocal imaging (e.g. Soeller *et al.* 2007), and it is a current challenge to construct detailed stochastic Ca²⁺ models that include these additional levels of local CRU gating complexity and SR geometry. With the development of even higher resolution imaging methods (Betzig *et al.* 2006; Juetz *et al.* 2008) data at the required nanometre scales should become experimentally accessible in the near future, although we note that tools

for simple model generation from quantitative imaging data still need further development.

Appendix: model equations and parameters

The evolution of Ca²⁺ is described by:

$$\frac{\partial[\text{Ca}^{2+}]}{\partial t} = \nabla(D_c \nabla[\text{Ca}^{2+}]) + J_{\text{sum}}$$

$$J_{\text{sum}} = J_{\text{RyR}} + J_{\text{buffers}} - J_{\text{pump}} + J_{\text{leak}}$$

where J_{sum} is the total Ca²⁺ flux per unit volume, which is the sum of contributions of release from RyR cluster (J_{RyR}), buffers (J_{buffers}), leak from SR (J_{leak}) and uptake by the sarcoplasmic reticulum Ca²⁺-ATPase pump (J_{pump}). These fluxes are calculated according to the following equations:

$$J_{\text{RyR}} = \sigma_{\text{RyR}} \delta(\vec{r}), \quad \sigma_{\text{RyR}} = \frac{i_{\text{Ca}}}{2F}$$

$$J_{\text{buffers}} = \sum_n J_n$$

$$J_{\text{pump}} = \frac{v_{\text{pump}} [\text{Ca}^{2+}]^m}{K_{\text{pump}}^m + [\text{Ca}^{2+}]^m}$$

$$J_{\text{leak}} = J_{\text{pump}}(C_0)$$

$$J_n = -\frac{[\text{Ca} B_n]}{\partial t}$$

$$= -k_n^+ [\text{Ca}^{2+}] ([B_n]_T - [\text{Ca} B_n]) + k_n^- [\text{Ca} B_n]$$

where n denotes the index of cytoplasmic buffers B_n , $\delta(\vec{r})$ is the delta function, σ_{RyR} the RyR flux magnitude, K_{pump}^m SR pump binding constant.

Ryanodine receptor clusters are spatially discrete, and their probability to fire is governed by a probability function, P , based on local Ca²⁺ concentration, and the Ca²⁺ sensitivity factor, K_{poss} , as follows:

$$P_{[\text{Ca}^{2+}]} = \frac{[\text{Ca}^{2+}]^n}{[\text{Ca}^{2+}]^n + K_{\text{poss}}^n}$$

The stochastic state function, S , for a RyR cluster defines the state of resting and firing, where T_N^M denotes the N th sparks at site M , and u_{rand} is a uniformly distributed

random number between 0 and 1, as follows:

$$S \in \{0, 1\}$$

$$S(P) = 1, \text{ if}$$

$$P_{[Ca^{2+}](\bar{r}_{N,t})} > u_{\text{rand}}, \quad \text{and} \quad T_N^M > T_N^{M-1} + \tau_R$$

Parameters were generally as described by Izu *et al.* (2001); see Tables 1 and 2. A notable exception are the diffusion parameters for Ca^{2+} , which were chosen to describe isotropic diffusion in accordance with recent data on isotropic spark properties (Bányász *et al.* 2007).

References

- Bányász T, Chen-Izu Y, Balke CW & Izu LT (2007). A new approach to the detection and statistical classification of Ca^{2+} sparks. *Biophys J* **92**, 4458–4465.
- Berlin JR, Cannell MB & Lederer WJ (1989). Cellular origins of the transient inward current in cardiac myocytes. Role of fluctuations and waves of elevated intracellular calcium. *Circ Res* **65**, 115–126.
- Bers DM (2001). *Excitation-Contraction Coupling and Cardiac Contractile Force*. Kluwer Academic Publishers, Dordrecht.
- Bers DM & Ginsburg KS (2007). Na:Ca stoichiometry and cytosolic Ca-dependent activation of NCX in intact cardiomyocytes. *Ann N Y Acad Sci* **1099**, 326–338.
- Betzig E, Patterson GH, Sougrat R, Lindwasser OW, Olenych S, Bonifacino JS, Davidson MW, Lippincott-Schwartz J & Hess HF (2006). Imaging intracellular fluorescent proteins at nanometer resolution. *Science* **313**, 1642–1645.
- Cannell MB, Cheng H & Lederer WJ (1994). Spatial non-uniformities in $[Ca^{2+}]_i$ during excitation-contraction coupling in cardiac myocytes. *Biophys J* **67**, 1942–1956.
- Chen-Izu Y, McCulle SL, Ward CW, Soeller C, Allen BM, Rabang C, Cannell MB, Balke CW & Izu LT (2006). Three-dimensional distribution of ryanodine receptor clusters in cardiac myocytes. *Biophys J* **91**, 1–13.
- Cheng H, Lederer MR, Lederer WJ & Cannell MB (1996). Calcium sparks and $[Ca^{2+}]_i$ waves in cardiac myocytes. *Am J Physiol Cell Physiol* **270**, C148–C159.
- Cheng H, Lederer WJ & Cannell MB (1993). Calcium sparks: elementary events underlying excitation-contraction coupling in heart muscle. *Science* **262**, 740–744.
- Cleemann L, Wang W & Morad M (1998). Two-dimensional confocal images of organization, density, and gating of focal Ca^{2+} release sites in rat cardiac myocytes. *Proc Natl Acad Sci USA* **95**, 10984–10989.
- Evans AM & Cannell MB (1997). The role of L-type Ca^{2+} current and Na^+ current-stimulated Na/Ca exchange in triggering SR calcium release in guinea-pig cardiac ventricular myocytes. *Cardiovasc Res* **35**, 294–302.
- Fabiato A (1983). Calcium-induced release of calcium from the cardiac sarcoplasmic reticulum. *Am J Physiol Cell Physiol* **245**, C1–C14.
- Fabiato A (1985). Time and calcium dependence of activation and inactivation of calcium-induced release of calcium from the sarcoplasmic reticulum of a skinned canine cardiac Purkinje cell. *J Gen Physiol* **85**, 247–289.
- Forbes MS, Hawkey LA & Sperelakis N (1984). The transverse-axial tubular system (TATS) of mouse myocardium: its morphology in the developing and adult animal. *Am J Anat* **170**, 143–162.
- Franzini-Armstrong C & Protasi F (1997). Ryanodine receptors of striated muscles: a complex channel capable of multiple interactions. *Physiol Rev* **77**, 699–729.
- Franzini-Armstrong C, Protasi F & Ramesh V (1999). Shape, size, and distribution of Ca^{2+} release units and couplons in skeletal and cardiac muscles. *Biophys J* **77**, 1528–1539.
- Izu LT, Means SA, Shadid JN, Chen-Izu Y & Balke CW (2006). Interplay of ryanodine receptor distribution and calcium dynamics. *Biophys J* **91**, 95–112.
- Izu LT, Wier WG & Balke CW (2001). Evolution of cardiac calcium waves from stochastic calcium sparks. *Biophys J* **80**, 103–120.
- Juette MF, Gould TJ, Lessard MD, Mlodzianoski MJ, Nagpure BS, Bennett BT, Hess ST & Bewersdorf J (2008). Three-dimensional sub-100 nm resolution fluorescence microscopy of thick samples. *Nat Methods* **5**, 527–529.
- Katra RP & Laurita KR (2005). Cellular mechanism of calcium-mediated triggered activity in the heart. *Circ Res* **96**, 535–542.
- Keizer J, Smith GD, Ponce-Dawson S & Pearson JE (1998). Saltatory propagation of Ca^{2+} waves by Ca^{2+} sparks. *Biophys J* **75**, 595–600.
- Kockskamper J, Sheehan KA, Bare DJ, Lipsius SL, Mignery GA & Blatter LA (2001). Activation and propagation of Ca^{2+} release during excitation-contraction coupling in atrial myocytes. *Biophys J* **81**, 2590–2605.
- Kong CH, Soeller C & Cannell MB (2008). Increased sensitivity of Ca^{2+} spark detection in noisy images by application of a matched filter object detection algorithm. *Biophys J* **95**, 6016–6024.
- Lakatta EG & Guarnieri T (1993). Spontaneous myocardial calcium oscillations: are they linked to ventricular fibrillation? *J Cardiovasc Electrophysiol* **4**, 473–489.
- Langer GA & Peskoff A (1996). Calcium concentration and movement in the diadic cleft space of the cardiac ventricular cell. *Biophys J* **70**, 1169–1182.
- Li P, Lancaster M & Holden AV (2007). A three dimensional ventricular E-cell (3Dv E-cell) with stochastic intracellular Ca^{2+} handling. In *Functional Imaging and Modeling of the Heart*, vol. LNCS 4466, ed. Sachse FB & Seemann G, pp. 180–189. Springer, New York.
- Lipp P & Niggli E (1993). Microscopic spiral waves reveal positive feedback in subcellular calcium signaling. *Biophys J* **65**, 2272–2276.
- Mori MX, Erickson MG & Yue DT (2004). Functional stoichiometry and local enrichment of calmodulin interacting with Ca^{2+} channels. *Science* **304**, 432–435.
- Olveczky BP & Verkman AS (1998). Monte Carlo analysis of obstructed diffusion in three dimensions: application to molecular diffusion in organelles. *Biophys J* **74**, 2722–2730.
- Page E, McCallister LP & Power B (1971). Stereological measurements of cardiac ultrastructures implicated in excitation-contraction coupling. *Proc Natl Acad Sci USA* **68**, 1465–1466.

- Pásek M, Simurda J, Orchard CH & Christé G (2008). A model of the guinea-pig ventricular cardiac myocyte incorporating a transverse-axial tubular system. *Prog Biophys Mol Biol* **96**, 258–280.
- Peterson BZ, DeMaria CD, Adelman JP & Yue DT (1999). Calmodulin is the Ca²⁺ sensor for Ca²⁺-dependent inactivation of L-type calcium channels. *Neuron* **22**, 549–558.
- Pratusevich VR & Balke CW (1996). Factors shaping the confocal image of the calcium spark in cardiac muscle cells. *Biophys J* **71**, 2942–2957.
- Soeller C & Cannell MB (1997). Numerical simulation of local calcium movements during L-type calcium channel gating in the cardiac diad. *Biophys J* **73**, 97–111.
- Soeller C & Cannell MB (1999). Examination of the transverse tubular system in living cardiac rat myocytes by 2-photon microscopy and digital image-processing techniques. *Circ Res* **84**, 266–275.
- Soeller C, Crossman D, Gilbert R & Cannell MB (2007). Analysis of ryanodine receptor clusters in rat and human cardiac myocytes. *Proc Natl Acad Sci USA* **104**, 14958–14963.
- Soeller C, Jacobs MD, Jones KT, Ellis-Davies GC, Donaldson PJ & Cannell MB (2003). Application of two-photon flash photolysis to reveal intercellular communication and intracellular Ca²⁺ movements. *J Biomed Opt* **8**, 418–427.
- Sperelakis N & Rubio R (1971). An orderly lattice of axial tubules which interconnect adjacent transverse tubules in guinea-pig ventricular myocardium. *J Mol Cell Cardiol* **2**, 211–214.
- Stern MD, Pizarro G & Rios E (1997). Local control model of excitation-contraction coupling in skeletal muscle. *J Gen Physiol* **110**, 415–440.
- Venetucci LA, Trafford AW, O'Neill SC & Eisner DA (2008). The sarcoplasmic reticulum and arrhythmogenic calcium release. *Cardiovasc Res* **77**, 285–292.
- Wussling MH & Salz H (1996). Nonlinear propagation of spherical calcium waves in rat cardiac myocytes. *Biophys J* **70**, 1144–1153.

Acknowledgements

This work was supported by grants from the Auckland Medical Research Foundation, the Health Research Council, the Wellcome Trust and the European Union through the Network of Excellence BioSim, Contract No. LHSB-CT-2004-005137. P.L. is a postdoctoral research fellow supported by the Center of Biomedical Computing at Simula Research Laboratory.